RSC Advances

ROYAL SOCIETY OF CHEMISTRY

www.rsc.org/advances

The Magnetism of Fe_4N/Oxides (MgO, $BaTiO_3$, $BiFeO_3$) Interfaces From First-Principles Calculations

Nan Feng[1], Wenbo Mi[1,*], Xiaocha Wang[2], Haili Bai[1]

[1]*Tianjin Key Laboratory of Low Dimensional Materials Physics and Preparation Technology, Faculty of Science, Tianjin University, Tianjin 300072, China*

[2]*Tianjin Key Laboratory of Film Electronic & Communicate Devices, School of Electronics Information Engineering, Tianjin University of Technology, Tianjin 300384, China*

[*]Author to whom all correspondence should be addressed.

E-mail: miwenbo@tju.edu.cn

ABSTRACT

The geometry, bonding, electronic and magnetic properties of Fe_4N/Oxides (MgO, $BaTiO_3$ and $BiFeO_3$) interfaces with different configurations are performed using the first-principles calculations. The *n*- and *p*-type doping of MgO are induced in Fe^IFe^{II}/MgO and $(Fe^{II})_2N$/MgO interfaces, respectively. The metallic characters are induced in $BaTiO_3$ by contact with Fe^IFe^{II} termination, followed by *p*-type doping in $(Fe^{II})_2N$/BaO interface and *n*-type doping in $(Fe^{II})_2N/TiO_2$ interface. The interfacial dipole due to charge rearrangement may induce the Fermi level pinning in Fe_4N/MgO and $(Fe^{II})_2N/BaTiO_3$ systems. The deposition of Fe_4N on $BiFeO_3$ leads to a metallic character of $BiFeO_3$ with the total magnetic moments of 0.33-1.54 μ_B. The different electronic and magnetic characters are governed by interfacial bonding between Fe_4N and oxides. These findings are useful for the future design of Fe_4N/oxides based spintronics devices.

Keywords: Fe_4N; Oxides; Electronic Structure; Magnetic Properties

PACS: 73.20.-r, 73.21.Ac, 74.20.Pq, 75.70.Cn

1. INTRODUCTION

Spintronics has the potential to give rise to the new-generation memory devices due to the possibility to manipulate the electron spin and charge degrees of freedom simultaneously.[1] From both fundamental and applications points of view, most of the interest currently focuses on systems like magnetic multilayers and dilute magnetic semiconductors, and so on.[2-5] Among them, the large tunneling magnetoresistance (TMR) observed in Magnetic tunnel junctions (MTJs) has attracted great interest due to its practical applications in spintronics devices, such as the magnetic sensors and magnetic random access memories.[6,7] MTJs are composed of two ferromagnetic electrodes separated by a thin insulating barrier layer. The ferromagnetic electrode serves as a spin-polarized injection source. The first understanding of TMR is the well-known Julliere's formula of TMR= $2P^2/\left(1+P^2\right)$, where P is the spin polarization of the ferromagnetic electrodes. Therefore, an electrode with a larger spin polarization can result in a larger TMR. However, the potential barrier between the ferromagnetic electrodes and insulator barrier can affect the magnitude and TMR sign, i.e., TMR also strongly depends on the mechanism of interfacial bonding. Therefore, it is important to study the electronic transport properties of the ferromagnet/insulator interfaces. Herewith, we focus on Fe_4N as an electrode because it has a large saturation magnetization, low coercivity and high chemical stability. The spin polarization and Curie temperature (T_C) of bulk Fe_4N are almost –100% and 761 K.[8,9] A TMR of –18.5% and –75% has been reported in the Fe_4N/MgO/CoFeB MTJs

fabricated by sputtering.[10,11] A negative spin polarization is observed in the monolayer MoS_2 by contact with Fe^{I}/Fe^{II} termination and *p*-type doping by contact with N termination of Fe_4N.[12] Therefore, Fe_4N is considered as a promising material for the practical application in spintronics devices.

Giant TMR has been observed in the CoFeB/MgO/CoFeB junctions with a TMR of 260% and 355% at room temperature,[13,14] which accelerates the application development for the MgO-based MTJs, because of their suitability to mass production. Besides the need for a large TMR, electrically controllable functionally is also highly desirable. The magnetoelectric coupling between the ferroelectricity and ferromagnetism allows the electric (magnetic) field control of magnetic (electric) properties. Since a prototype single-phase multiferroic material suitable for industrial applications has not been emerged so far, the composite multiferroics, where a ferroelectric or multiferroic layer is interfaced with a ferromagnetic layer, has been intensively studied.[15,16] $BaTiO_3$ is a prototypical perovskite-like ferroelectric oxide,[17] which shows a high ferroelectric T_C of 400 K. The magnetoelectric effect between ferromagnet and $BaTiO_3$ has been studied.[18-21] Otherwise, bulk $BiFeO_3$ is the only known single-phase multiferroic material with a high ferroelectric T_C of 1103 K and high G-type antiferromagnetic Néel temperature of 643 K.[22,23] Béa and Ju have used the multiferroic $BiFeO_3$ epitaxial films as a tunnel barrier in MTJ.[24,25] The magnetic configuration in MTJ can be changed from parallel to antiparallel as an electric field is applied due to the strong ferroelectricity with a large spontaneous electric polarization in $BiFeO_3$. Therefore, it is interesting to combine these materials to form

the ferromagnetic/ferroelectric heterostructures, which will promote the more efforts to design multifunctional devices.

MgO, $BaTiO_3$ and $BiFeO_3$ are three typical materials for different kinds of tunnel barrier, traditional, ferroelectric, multiferroic, respectively, which can be used for classic, ferroelectric and spin filter junctions. The purpose of this work is to give a clear picture of the interfacial coupling mechanism at the Fe_4N/Oxides (MgO, $BaTiO_3$ and $BiFeO_3$) interfaces and its effect on the magnetic and electronic properties of the interfaces. Meanwhile, one can determine which oxide can be a reasonable insulating barrier in MTJs with Fe_4N as an electrode. Our results demonstrate that the *n*- and *p*-type MgO are induced in the $Fe^{I}Fe^{II}$/MgO and $(Fe^{II})_2N$/MgO interfaces, respectively. The metallic characters are induced in $BaTiO_3$ by contact with $Fe^{I}Fe^{II}$ termination, whereas the *p*-type doping in $(Fe^{II})_2N$/BaO interface and *n*-type doping in $(Fe^{II})_2N/TiO_2$ interface appear. The large deviation of the calculated Schottky barrier heights at the Fe_4N/MgO and $(Fe^{II})_2N/BaTiO_3$ interfaces from the prediction of the classical Schottky barrier heights suggests the presence of Fermi level pinning by the formation of interfacial dipole. The deposition of Fe_4N on $BiFeO_3$ can result in a metallic $BiFeO_3$. The different interfacial bonding between the Fe_4N and oxides leads to the different electronic and magnetic properties.

2. CALCULATION DETAILS AND MODEL

Our first-principles calculations are based on density functional theory[26] and

projector augmented wave methods[27] as implemented in Vienna Ab initio Simulation Package.[28] The Perdew-Burke-Ernzerhof[29] spin-polarized generalized gradient approximations are used as exchange-correlation potential. The projector augmented wave potentials are used to describe the electron-ion interaction with the following valence-electron configurations: Fe $3d^7 4s^1$, N $2s^2 2p^3$, Mg $2p^6 3s^2$, O $2s^2 2p^4$, Ba $5p^6 6s^2$, Ti $3d^3 4s^1$, Bi $6s^2 6p^3$. In all the supercells of Fe_4N/oxides studied here, a 15-Å vacuum space in z-direction is introduced to separate the interaction between periodic images. The plane-wave cutoff is set to 500 eV and the Brillouin-Zone samplings with 9×9×9 and 9×9×1 k mesh are used for bulk Fe_4N, oxides and Fe_4N/oxides interfaces, respectively. All structures are fully optimized until the force on each atom is less than 0.01 eV/Å and total energy is converged to 10^{-5} eV. Since the magnetic oxides are generally thought to be strongly correlated materials, as for the calculations of the electronic structure of $BiFeO_3$ and Fe_4N/$BiFeO_3$ interface, a density function plus U scheme is employed to account for the strong electron correlations, in which an effective on-site interaction parameter $U_{eff}=U-J$ incorporates the on-site Coulomb (U) and the exchange interaction (J). An equivalent interpretation of this scheme would be to consider J=0 and treat $U_{eff}=U$ as only parameter in this work. We set only U=4.5 eV for Fe d orbital in $BiFeO_3$ component based on our previous electronic structural calculations of bulk $BiFeO_3$ and Fe_3O_4/$BiFeO_3$ superlattice.[30] We have confirmed that our adopted U value is sufficient to describe the magnetic moment of Fe atoms, antiferromagnetic ordering, ferroelectricity and the density of states of bulk $BiFeO_3$.

Bulk Fe_4N has a cubic perovskite-type structure ($Pm3m$) with a lattice constant

of a=3.795 Å. In its lattice, two types of Fe atoms occupy the corner (Fe^{I}) and face-centered sites (Fe^{II}), and N atom locates at the body-centered position. Fe^{I} atom is surrounding by 12 Fe^{II} atoms with a distance of $a/\sqrt{2}$ as the nearest neighbors, Fe^{II} atom has two N atoms at a/2 as the nearest neighbors and 12 Fe^{I} atoms as the second nearest neighbors.[31] For MgO, $BaTiO_3$ and $BiFeO_3$, we study the rocksalt structure with a space group of *Fm*3*m*, cubic perovskite structure with space group *Pm*3*m* and tetragonal structure with space group *P*4*mm*, respectively. MgO consists of two interpenetrating face-centered cubic lattices of Mg and O atoms. In the cubic unit cell of $BaTiO_3$, there is one Ba atom at the origin (0.0, 0.0, 0.0)a, one Ti atom at the body center (0.5, 0.5, 0.5)a and three O atoms at the three face centers (0.5, 0.5, 0.0)a, (0.0, 0.5, 0.5)a and (0.5, 0.0, 0.5)a. The experimental lattice parameters of MgO and $BaTiO_3$ are 4.211 and 4.010Å, respectively,[32,33] i.e., the lattice mismatches with Fe_4N (3.795Å) are 10.4% and 5.5%, respectively. Even though the large lattice mismatch is present, the epitaxial Fe_4N/MgO heterostructures have been fabricated experimentally.[34] We choose a tetragonal ferroelectric $BiFeO_3$ as substrate mainly because the Fe_4N(001) can nicely match with (001) plane of the tetragonal structure with a mismatch of about 3.6%. Furthermore, based on the experimental results, the tetragonal $BiFeO_3$ is stabilized by being placed on the lattice-matched substrates and its spontaneous polarization (63.2 μC/cm^2) is significantly higher than that of rhombohedral structure (6.61 μC/cm^2).[35] The tetragonal $BiFeO_3$ has a lattice constant of a=3.935 Å and c/a=1.016.[36] The primitive cell of tetragonal $BiFeO_3$ contains one molecule with one Bi atom sitting at (0.0, 0.0, 0.0)a, one Fe atom at (0.5, 0.5, 0.41)a,

one axial O1 atom at (0.5, 0.5, –0.12)*a* and two equatorial O2 atoms at (0.0, 0.5, 0.34)*a* and (0.5, 0.0, 0.34)*a*. The antiferromagnetic character of G-type or C-type has not been clear in the tetragonal phase film. In this work, we only consider the G-type antiferromagnetic tetragonal $BiFeO_3$, where the Fe atoms are coupled ferromagnetically within the (111) planes and antiferromagnetically between adjacent planes.[37]

The Fe_4N/oxides interfaces are simulated by building up supercells consisting Fe_4N(001) layers on the top of oxide(001) layers. For the lattice mismatch, we adopt the average lattice constant of Fe_4N and oxides for the *ab*-plane of our supercells. For $Fe_4N/BaTiO_3$ interface, the in-plane lattice constant is 3.902 Å, which is smaller than the theoretical lattice constant of the cubic phase of $BaTiO_3$ (4.010 Å). By analogy with $Fe/BaTiO_3$ multilayers, $BaTiO_3$ in our calculations is also assumed to have a tetragonal structure, which is well known experimentally to be stable at room temperature.[18,38,39] We choose $Fe^{I}Fe^{II}$ and $(Fe^{II})_2N$ surface terminations of Fe_4N(001) at interfaces, respectively. As for oxides, the MgO, BaO, TiO_2, BiO and FeO_2 terminations are considered. For Fe_4N/MgO supercells: models a and b contain the interface of $Fe^{I}Fe^{II}$-MgO and $(Fe^{II})_2N$-MgO, respectively. For $Fe_4N/BaTiO_3(BiFeO_3)$ supercells: model a contains the $Fe^{I}Fe^{II}$-BaO(BiO) interface; model b contains the $Fe^{I}Fe^{II}$-$TiO_2(FeO_2)$ interface; model c contains the $(Fe^{II})_2N$-BaO(BiO) interface; model d contains the $(Fe^{II})_2N$-$TiO_2(FeO_2)$ interface, see Fig. 1.

The most stable structure among the different interfaces is determined by calculating the cohesive energy between Fe_4N and oxides, $E_{coh} = E_{comb} - E_{Fe_4N} - E_{oxide}$,

where E_{comb}, E_{Fe_4N} and E_{oxide} represent the total energy of the relaxed Fe_4N/oxides interfaces, Fe_4N and oxide slabs, respectively. For further illustrating the detailed nature of the charge transfer at the Fe_4N/oxides interfaces, we calculate the charge density difference, which is obtained by subtracting the charge densities of the isolated Fe_4N and oxide slabs from the total charge density in the supercells. The electronic structures of the isolated Fe_4N and oxide slabs are calculated by freezing the atomic positions of the respective components as obtained in the supercells. To have a quantitative picture, the induced charge transfer q is estimated by integrating $\Delta\rho(z)$ over the full z range, where $\Delta\rho(z)$ is the plane-averaged charge density difference along the direction perpendicular to the interfaces. The work function (W) is defined by the lowest energy required to remove an electron deep inside bulk. It is defined as $W = V(\infty) - E_F$, where $V(\infty)$ is the electrostatic potential in the middle of the vacuum region and E_F is Fermi energy of the slab. Taking $(Fe^{II})_2N$/MgO and $(Fe^{II})_2N/TiO_2$ as examples, the dipole correction has been checked, and the detailed results indicate that it has only negligible influence on the electronic structure and magnetism of Fe_4N/oxides interfaces.

3. RESULTS AND DISSCUSIONS

For bulk Fe_4N, we obtain a lattice constant of 3.795 Å, which agrees well with the experimental value.[8] The calculated average magnetic moments of Fe^{I}, Fe^{II} and N are 2.95, 2.31 and 0.02 μ_B, respectively, which are in accordance with previous

theoretical and experimental results.[40-44] The shaded plots in Fig. 2 present the partial density of states (PDOSs) for bulk Fe_4N and MgO. The shaded plots for bulk are also used in other figures. For Fe^{I}, Fe^{II} and N [Fig. 2(a)], a distinct spin splitting of Fe *d* states appears, which induces the ferromagnetism. The DOS of Fe_4N at E_F is mainly from the minority spin channel. From –8.5 to –5 eV, the N *p* states strongly hybridize with the Fe^{II} *d* states to form covalent bonds, whereas in the same energy region the Fe^{I} *d* states show hardly any hybridization with N. Thus, the Fe^{II} magnetic moment is smaller than Fe^{I}. The bulk band gaps in our calculation are 4.5, 1.7 and 1.9 eV for three oxides, respectively, which shows a good agreement with previous calculations.[45,32,30] The gap is somewhat lower than the experimental band gap of 7.8 eV for MgO, 3.2 eV for $BaTiO_3$, and 2.5 eV for $BiFeO_3$.[46,32,47] The origin of the discrepancy may be well known as the failures of density functional theory in correctly describing the excited states, the band gaps are strongly underestimated even for insulators. We believe that the results presented here are nevertheless likely to be qualitatively correct. The calculated Fe magnetic moment in bulk $BiFeO_3$ is ±4.18 μ_B/atom, which is identical to the previous reported value.[36]

Usually, the appearance of Fe magnetic moments in Fe_4N is attributed to the symmetry breaking: N is located at the body-centered position of the nonmagnetic face-centered cubic Fe. Therefore, the enhancement of Fe magnetic moments should also be related to the symmetry. Since the magnetic moment mainly originates from the unpaired *d* electrons and the hybridization between Fe and other atoms can reduce the amount of unpaired *d* electrons, it is the hybridization that determines the spin

polarization of Fe_4N layer.[48]

3.1 Fe_4N/MgO Interfaces

Initially we examine the energetic stability and the equilibrium geometry of the Fe_4N/MgO interfaces. The calculated interfacial cohesive energies are –1.72 and –1.28 eV for models a and b, respectively, indicating that the former is more stable. The equilibrium bond length of O-Fe^{I}(Fe^{II}) is 2.34(2.02) Å for model a, while that of Mg(O)-Fe^{II}(N) is 4.13(3.76) Å for model b, confirming that the $(Fe^{II})_2$N-MgO interaction is weak and the Fe_4N lattice structures are perturbed upon the presence of MgO for both the systems due to the relatively large lattice mismatch.

In Table I, the magnetic moments of Fe_4N and MgO in the Fe_4N/MgO interfaces are presented. As compared to bulk Fe_4N, the magnetic moment of Fe_4N decreases by 13.7% for model a, while it slightly increases for model b. The broken symmetry at a surface or interface[49] makes the Fe magnetic moments in layers I and III increase as compared to bulk. However, the strong hybridization between Fe and MgO can weaken it. Therefore, the Fe magnetic moments in layer I are slightly smaller than layer III. Fig. 2 shows the PDOSs of models a-b. The label I, for example, refers to layer I, as defined in Fig. 1, and Fe^{II} denotes Fe atoms at the face-centered sites (which will be distinguished by numbers in round brackets). The same definition is used in other figures. For model a, the Fe^{I} magnetic moment in layer I is almost identical with layer III. A smaller Fe^{II} magnetic moment in layer I can be attributed to

the strong hybridization with O in layer I in the energy range from –7.61 to –5.65 eV. A large overlap can be seen in the energy range from –2.34 to 6.70 eV, as shown in Figs. 2(a) and (b). Smaller/larger Fe^{II} magnetic moments in layer II are the consequence of stronger/weaker hybridization with N in layer II in the energy range from –3.66 eV to E_F. The hybridization induces a small magnetic moment of 0.02 μ_B in MgO for model a. For model b, the hybridization appears between N in layer I and O in layer I, whereas Fe^{II} has hardly any hybridization with O because of the large distance. The reduced Fe^{I} magnetic moment in layer II is due to the appearance of hybridization with N in layers I and III in the energy range from –2.81 to 4.44 eV. As N in layers I and III strongly hybridize with Fe^{II} in layer II in the energy range from –6.77 to –3.36 eV, Fe^{II} magnetic moment is slightly smaller than bulk.

Fig. 3 gives the band structures for the spin-unpolarized MgO and the supercells, demonstrating the changes of the electronic states in MgO upon interface formation. The red color represents the contribution of MgO in the supercells. We observe that the band gap of MgO decreases to 3.93 and 3.53 eV for models a and b, respectively. The E_F of the supercell always lies in the band gap of MgO, resulting in the formation of a Schottky barrier at the interface. The barrier height is defined by the energy difference between the metal's Fermi level and the semiconductor's VB maximum (*p*-type barrier) or CB minimum (*n*-type barrier). Figs. 3(b)-(e) show that the *n*-type ($\Phi_{B,n}$) and *p*-type ($\Phi_{B,p}$) Schottky barrier heights, which are calculated to be 1.02 and 0.76 eV for models a and b, respectively. A classical Schottky junction fulfills $\Phi_{B,n} = \Phi_M - \chi_s$, $\Phi_{B,p} = E_g - \Phi_{B,n}$, where E_g and χ_s are the band gap and electron

affinity of the semiconductor, and Φ_M is the work function of the metal. Due to the above mentioned limitation of the generalized gradient approximation to reproduce the band gap, we use the experimental value for the band gap as a good approximation. From the vacuum potential and E_F, we have obtained a value of Φ_M= 4.30, 4.55 eV for $Fe^{I}Fe^{II}$- and $(Fe^{II})_2N$-terminated surface of $Fe_4N(001)$, respectively. The work function of MgO(001) is about 4.77 eV, so the derived χ_s is about 0.87 eV and is consistent with a reported value of 0.85 eV.[46] This leads to $\Phi_{B,n}$=3.43 eV and $\Phi_{B,p}$=4.12 eV, respectively, which deviates from the value derived from the band structure, reflecting a rather strong Fermi level pinning. It is well known that the TMR is a spin-dependent tunneling effect. The appearance of Schottky barriers at Fe_4N/MgO interfaces verifies that the electron from Fe_4N electrode must tunnel through MgO insulating layers, which is a necessary condition for the presence of TMR effects in the previous reported Fe_4N/MgO/CoFeB MTJs.[10,11]

The charge transfer at the interfaces is quantified by charge density difference calculations (see Fig. 1), showing that charge is lost from the Fe^{II} and O atoms, while it accumulates in the Fe^{II}-O bond region, reflecting the covalent bonding across the interface for model a. It is worth noting that some extra charge accumulates around N. For model b, the depleted charge from N and O mainly concentrates at the N-O region. The plane-averaged charge difference analysis is performed to zoom into the details at the interfacial region. Both the charge depletion and accumulation can be observed at the interface, suggesting the interfacial charge redistribution, that is, the formation of the interfacial electric dipole. Therefore, the formation of Fermi level pinning may be

as a result of the presence of interfacial dipole effect.[50] The metal induced gap states[51] and surface states[52] also may have contributions to the Fermi level pinning. Furthermore, the charge redistribution in model a is much more pronounced than model b, resulting in a stronger interaction.

3.2 $Fe_4N/BaTiO_3$ Interfaces

The cohesive energies and bond lengths in four models of the $Fe_4N/BaTiO_3$ interfaces are listed in Table II. The stability order is found to be b<c<a<d, see Fig. 1. The energetically favorable case is d, i.e., the interfacial Fe^{II}(N) located on the top of O(Ti). The large E_{coh}=–2.31 eV is from the strong Ti-N bonds with a bond strength of 2.03 Å.

Table III gives the magnetic moments of Fe_4N and $BaTiO_3$ in the $Fe_4N/BaTiO_3$ systems, the Fe_4N magnetic moments are subject to reductions of 0.63%, 3.65% and 4.69% as compared to bulk Fe_4N for models b-d, respectively. However, the Fe_4N magnetic moment in model a is slightly enhanced by 2.23%. The Fe magnetic moments in layers I are different from layer III, reflecting the interfacial coupling with $BaTiO_3$. Except for model a, the Fe magnetic moments in layer I are slightly enhanced as compared to bulk, as previously demonstrated that in the $Fe/BaTiO_3$ superlattice and $Fe_3O_4/BaTiO_3$ heterostructure.[18,19] The Fe magnetic moment in layer II is smaller than bulk due to the enhanced hybridization with the nearest N.

Fig. 4 gives the PDOSs of models a-b. For model a, as can be seen from Figs. 4(a)

and (b), the Fe^{I} in layer I hybridizes with O in layer I in the energy range from –2.60 to –1.66 eV and E_F to 4.15 eV. Furthermore, the hybridization between Fe^{I} and N in layer II appears in the energy range from –3.13 to –1.51 eV, which reduces the magnetic moment, as shown in Table III. The Fe^{II} strongly hybridizes with O in the energy range from –7.43 to –0.65 eV and E_F to 4.15 eV, resulting in a larger Fe^{II} magnetic moment than bulk, but smaller than layer III. The PDOS indicates that the Fe^{II} in layer II strongly hybridizes with N in layer II over a wide energy range from –5.18 to 4.84 eV, resulting in a reduced Fe^{II} magnetic moment as compared to bulk. The induced magnetic moments of interfacial O and Ba are about 0.11 and 0.02 μ_B, respectively and are parallel to that of Fe^{I}/Fe^{II}. By contrast, the magnetic moment of Ti is 0.05 μ_B and antiparallel to Fe^{I}/Fe^{II}, which is attributed to that the hybridization with Fe^{I}/Fe^{II} in the energy range from the –0.55 to 1.91 eV makes the minority-spin states of Ti have a greater occupation than the majority-spin states. Strong orbital overlap between Fe^{I}/Fe^{II} and O, Ti induces a metallic character of $BaTiO_3$. To analyze the case of the spin polarization (P) at E_F, P is defined as $P=\left[N_{\uparrow}(E_F)-N_{\downarrow}(E_F)\right]\Big/\left[N_{\uparrow}(E_F)+N_{\downarrow}(E_F)\right]$, in terms of the total DOS in the majority spin $N_{\uparrow}$ and minority spin channels $N_{\downarrow}$, respectively. We find P=–27.5% deriving from Fig. 4(b) and the value has the same sign of spin-polarization with Fe_4N, indicating that the carrier polarization is not inversed. The PDOS of model b is shown in Figs. 4(c) and (d). As compared to model a, Fe^{I} in layer I shows hardly any hybridization with N in layer II, so its magnetic moment is larger than that in model a. The enhanced hybridization between Fe^{I} in layer III and N in layer II makes its magnetic

moment smaller than bulk. The hybridization between the Fe^{I}/Fe^{II} and Ti appears in the energy range from –0.84 to E_F and causes a charge redistribution between majority- and minority-spin states, giving rise to a large antiparallel magnetic moment on the interfacial Ti atom (–0.25 μ_B). The induced O magnetic moment (0.05 μ_B) is relatively small because of less hybridization with Fe^{I}/Fe^{II} in the same energy range. The P is found to be –9.6%.

Fig. 5 gives the PDOSs of models c-d. For model c, it is clear that the N electronic states are similar in layers I and III due to the weak interactions with $BaTiO_3$. The Fe^{II} magnetic moment in layer I slightly decreases as compared to layer III, which can be attributed to the hybridization with O in layer I in the energy range from –2.57 to 0.22 eV, as shown in Figs. 5(a) and (b). The Fe^{I} magnetic moment in layer II decreases because of the enhanced hybridization with N in layer I in the energy range from –3.02 to 3.02 eV. The weak interfacial bonding induces a small O magnetic moment of 0.01 μ_B. For model d, the interfacial bonding is similar to model b. One can see the hybridization between Fe^{II} in layer I and O in layer I in the energy range from –8.05 eV to E_F, as shown in Figs. 5(c) and (d). The hybridization induces an O magnetic moment of 0.04 μ_B. The induced magnetic moment of Ti atom is –0.03 μ_B, which is ascribed to the hybridization with Fe^{II} in the energy range from –1.66 to 0.67 eV. In the energy range from –7.84 to –0.78 eV, the hybridization appears between N in layer I and Ti in layer I. The magnetic moments obtained for $BaTiO_3$ in models a-d are 0.08, –0.19, 0.01 and 0.07 μ_B, respectively.

Fig. 6 shows the spin-polarized band structures of the $Fe_4N/BaTiO_3$ interfaces.

Energy level splitting occurs between the majority and minority spin channels near E_F, which induces magnetic moments of $BaTiO_3$. For model a, the majority and minority spin CB minimum shifts down across E_F, showing a metallic feature. For model b, the interaction between Fe_4N and $BaTiO_3$ is weak as compared to model a, the induced metallicity is not apparent. The $BaTiO_3$ in model c can be regarded as *p*-type doping with a gap of 1.91 eV, as E_F of the supercell locates at VB maximum of $BaTiO_3$. As for model d, E_F is situated at the position of 0.72 eV above VB maximum and 0.10 eV below CB minimum of $BaTiO_3$, indicating the *n*-type doping. Meanwhile, the band gap decreases to 0.80 eV and a $\Phi_{B,n}$ of 0.10 eV is observed. The work functions of BaO- and TiO_2-terminated (001) surfaces are well established as 2.37 and 5.40 eV, so the electron affinities are 0.77 and 3.80 eV, respectively. The classical Schottky barrier heights are –0.58 and 0.77 eV, which are different from the values derived from the band structure.

The charge density differences for the $Fe_4N/BaTiO_3$ interfaces are also shown in Fig. 1. For model a, Fe^{II} in layer I and Ti in layer II lose charge, while a slight but significant accumulation around the interfacial O atom and some extra charge is also found to accumulate around interfacial Fe^{I} atom, which indicates that the interfacial bonding between the $Fe^{I}Fe^{II}$ and BaO surface takes on the ionic nature. As for model b, charge is lost from Fe^{II} and Ti atoms, while it accumulates in the Fe^{II}-Ti bond region, reflecting a covalent bonding across the interface. The charge density difference plot in model c shows that the charge density distribution at the $(Fe^{II})_2N$-BaO interfacial layer is small, reflecting that the interfacial interaction is

rather weak. We can see charge accumulation around the interfacial Fe^{II} atoms and charge depletion at O atoms. Therefore, the *p*-type doping of $BaTiO_3$ on the $(Fe^{II})_2N$-terminated surface of $Fe_4N(001)$ is due to the electron transfer from $BaTiO_3$ to Fe_4N. The charge density difference map in model d demonstrates that the electronic interactions at the $(Fe^{II})_2N$-TiO_2 interfacial layer are characterized by strong covalent bonding among Fe^{II}, O, N, and Ti. The interfacial charge redistribution occurs in models c and d, indicating that the Fermi level pinning may originates from the dipole effect that exists at $(Fe^{II})_2N/BaTiO_3$ interfaces.

3.3 $Fe_4N/BiFeO_3$ Interfaces

The models b, c and d in the $Fe_4N/BiFeO_3$ interfaces have a positive cohesive energy, implying the formation of these interfaces is an endothermic process and thermodynamically unstable. It is also indicated by the large distance between the Fe_4N and $BiFeO_3$ (see the respective bond lengths in Table II). The strongest cohesion between the Fe_4N and $BiFeO_3$ is exhibited by model a, i.e., the BiO-terminated surface with interfacial $Fe^{I}(Fe^{II})$ lying on the top of the interfacial Bi(O1) atoms, as given in Fig. 1.

Table IV gives the magnetic moments of Fe_4N and $BiFeO_3$ in the $Fe_4N/BiFeO_3$ interfaces. The Fe_4N magnetic moments decrease by 1.54%, 5.13%, 32.72% and 5.20% as compared to bulk Fe_4N for models a-d, respectively. The PDOSs of models a-b are addressed in Fig. 7. For model a, as can be shown in Figs. 7(a) and (b) that the

hybridization between Fe^{I} in layer I and Bi in layer I in the energy range from –2.62 to 0.82eV and the enhanced hybridization between Fe^{I} and N in layer II reduce the Fe^{I} magnetic moment. The hybridization between Fe^{II} in layer I and O1 in layer I in the energy range from –1.09 to 2.10 eV makes the spin splitting of Fe between the majority and minority spin channels become stronger, resulting in a larger Fe^{II} magnetic moment than bulk, but smaller than layer III. The enhanced hybridization between Fe^{II} in layer II and N in layer II in the energy range from –4.24 to 4.10 eV leads to a smaller Fe^{II} magnetic moment as compared to bulk. The PDOS of O1 on all the atomic layers is relatively symmetrical, in accord with the reduced O1 magnetic moment. Furthermore, there are two kinds of O1 atoms in layer I with different magnetic moments, which is due to the facts that O1 with a larger magnetic moment has a weaker hybridization with Bi in layer I than O1 with a smaller magnetic moment. The Fe magnetic moments in $BiFeO_3$ on all the atomic layers have only a small change as compared with bulk $BiFeO_3$. Figs. 7(c) and (d) show the PDOS of model b. The reduction of the electronic states of Fe in layer I indicates that the corresponding Fe magnetic moment decreases as compared to bulk $BiFeO_3$, due to the hybridization with Fe^{II} in layer I in the energy range from –3.76 to –1.38 eV. The electronic states of Fe in layer V have a strong spin-splitting behavior and produce spin-polarized carriers at Fermi level, leading to a local net magnetic moment of 1.01 μ_B. The Fe(4) magnetic moment is reduced to –3.11 μ_B, which is from the enhanced hybridization with O2 in layer V as compared to bulk $BiFeO_3$. The Fe^{II}-Fe interfacial bonding induces no significant Bi magnetic moment (0.01 μ_B).

Fig. 8 shows the PDOSs of models c and d. In model c, the hybridization between Fe^{II} in layer I and Bi in layer I appears in the energy range from –0.14 to 4.92 eV. The Fe^{II}-Bi interfacial bonding makes the Fe^{II} magnetic moments on all the atomic layers decrease, where the magnetic moments of Fe^{II} further away from the interface are larger, as shown in Table IV. The electronic states of Fe of $BiFeO_3$ in layers II and IV show a strong spin-splitting, resulting in a local net magnetic moment of –0.83 and 0.60 μ_B, respectively, which can be ascribed to the interfacial bonding. There are two kinds of Fe atoms with different magnetic moments in layers II and IV, which may be from the facts that Fe atoms with small magnetic moments have a stronger hybridization with the nearest O2 atom near E_F. There are two kinds of O1 atoms with different magnetic moments on all the atomic layers, which may be due to the facts that O1 with small magnetic moments have a stronger hybridization with the nearest Bi atoms. The hybridization between Fe^{I} in layer II and N in layers I, III in the energy range from –4.46 to –0.80 eV makes the Fe^{I} magnetic moment decrease. For model d, the hybridization between Fe^{I} in layer II and N in layers I, III in the energy range from –4.14 to 1.73 eV reduces the Fe^{I} magnetic moment. The hybridization appears between Fe^{II} in layers I, III and O2 in layer I, resulting in a slight increase of corresponding Fe^{II} magnetic moments as compared to bulk. The reduced Fe^{II} magnetic moment in layer II is attributed to the enhanced hybridization with N in layers I, III in the energy range from –8.16 to –3.80 eV and the hybridization with O2 in layer I. The Fe^{II}-O2 interfacial bonding makes the O2 magnetic moment in layer I up to 0.13 μ_B. The Fe magnetic moments of $BiFeO_3$ in layers I and III have only a

small change, but that of Fe(4) in layer V reduced to –3.65 μ_B and the net Fe magnetic moment is 0.51 μ_B because of a stronger hybridization with O2 in layer V. The total magnetic moments of $BiFeO_3$ in models a-d are –0.33, 1.54, 0.59 and –0.46 μ_B, respectively. Strong orbital hybridization induces a metallicity of $BiFeO_3$. The spin polarization can be derived from Figs. 7 and 8 as P=33.3%, –34.5%, –19.9% and –7.7% for $BiFeO_3$ in models a-d, respectively. The change in the sign of the spin polarization at E_F is related to the hybridization mentioned above.

The band structures of the $Fe_4N/BiFeO_3$ systems are plotted in Fig. 9. The majority and minority spin bands are asymmetric for $BiFeO_3$ in four models. For models a, c and d, $BiFeO_3$ bands strongly hybridize with Fe_4N, inducing a metallic character of $BiFeO_3$. For model b, the weak interaction between Fe^IFe^{II} and FeO_2 also induces the metallicity of $BiFeO_3$. Therefore, $BiFeO_3$ cannot be used for the tunnel barrier in MTJs with Fe_4N as an electrode.

The charge redistribution between Fe_4N and $BiFeO_3$ is also shown in Fig. 1, showing the formation of bonds. Since there is no obvious charge density accumulation in Fe^I-Bi, Fe^{II}-O1, or Fe^{II}-Fe bonding regions, we obtain an ionic-like bonding picture for modes a-b, with the charge transfer and polarization. In model c, a depletion of Fe^{II} charge density on all the atomic layers is observed and the charge from Fe^{II} atom in layer I is transferred more to Bi in layer I. For model d, clearly, there is significant charge transfer from O2 in layer I to Fe^{II} in layer I.

4. CONCLUSION

The main findings of our first-principles calculations on the Fe_4N/Oxides interfaces can be summarized as follows: (1) The deposition of Fe_4N on MgO can lead to *n*- and *p*-type doping of MgO, depending on the $Fe^{I}Fe^{II}$ and $(Fe^{II})_2N$ contacted terminations of $Fe_4N(001)$, respectively. (2) Both effects are found in $BaTiO_3$, where in contact with $Fe^{I}Fe^{II}$ termination gives rise to metallic characters, whereas in contact with $(Fe^{II})_2N$ termination preserves semiconducting characters. Furthermore, *p*-type doping is found in $(Fe^{II})_2N$/BaO interface and *n*-type doping in the $(Fe^{II})_2N/TiO_2$ interface. Magnetic moments of 0.01-0.19 μ_B are detected. (3) We assume that the dipole effect which exists at the Fe_4N/MgO and $(Fe^{II})_2N/BaTiO_3$ interfaces may cause Fermi level pinning so that the calculated Schottky barrier heights are different from classical Schottky barrier heights. (4) The deposition of Fe_4N on $BiFeO_3$ can lead to conductive $BiFeO_3$ with total magnetic moment of 0.33-1.54 μ_B. The different electronic and magnetic characters are a consequence of interfacial bonding between Fe_4N and oxides. We hope that the work described here can serve as a theoretical foundation for further experimental investigation on Fe_4N/oxides based spintronics devices.

ACKNOWLEDGEMENTS

W. B. M. was supported by the National Natural Science Foundation of China (51171126), Key Project of Natural Science Foundation of Tianjin City

(12JCZDJC27100), Program for New Century Excellent Talents in University (NCET-13-0409) and Scientific Research Foundation for the Returned Overseas Chinese Scholars, State Education Ministry of China.

REFERENCES

1 S. Wolf, D. Awschalom, R. Buhrman, J. Daughton, S. von Molnar, M. Roukes, A. Chtchelkanova and D. Treger, *Science*, 2001, **294**, 1488.

2 C. Chen and W. Hsueh, *Appl. Phys. Lett.*, 2014, **104**, 042405.

3 G. Xing, J. Yi, F. Yan, T. Wu and S. Li, *Appl. Phys. Lett.*, 2014, **104**, 202411.

4 J. Lee, G. Xing, J. Yi, T. Chen, M. Lonescu and S. Li, *Appl. Phys. Lett.*, 2014, **104**, 012405.

5 D. Wang, G. Xing, F. Yan, Y. Yan and S. Li, *Appl. Phys. Lett.*, 2014, **104**, 022412.

6 I. Zutić, J. Fabian and S. Sarma, *Rev. Mod. Phys*., 2004, **76**, 323.

7 E. Tsymbal, O. Mryasov and P. LeClair, *J. Phys.: Condens. Matter*, 2003, **15**, R109.

8 S. Kokado, N. Fujima, K. Harigaya, H. Shimizu and A. Sakuma, *Phys. Rev. B*, 2006, **73**, 172410.

9 S. Nagakura, *J. Phys. Soc. Jpn.*, 1968, **25**, 488.

10 K. Sunaga, M. Tsunoda, K. Komagaki, Y. Uehara and M. Takahashi, *J. Appl. Phys.*, 2007, **102**, 013917.

11 Y. Komasaki, M. Tsunoda, S. Isogami and M. Takahashi, *J. Appl. Phys.*, 2009, **105**, 07C928.

12 N. Feng, W. Mi, Y. Cheng, Z. Guo, U. Schwingenschlögl and H. Bai, *ACS Appl. Mater. Interfaces*, 2014, **6**, 4587.

13 J. Hayakawa, S. Ikeda, F. Matsukura, H. Takahashi and H. Ohno, *Jpn. J. Appl. Phys*., Part 2 2005, **44**, L587.

14 S. Ikeda, J. Hayakawa, Y. Lee, R. Sasaki, T. Meguro, F. Matsukura and H. Ohno, *Jpn. J. Appl. Phys.,* Part 2 2005, **44**, L1442.

15 W. Eerenstein, M. Wiora, J. Prieto, J. Scott, N. Mathur, *Nat. Mater*., 2007, **6**, 348.

16 H. Tian, T. Qu, L. Luo, J. Yang, S. Guo, H. Zhang, Y. Zhao, J. Li, *Appl. Phys. Lett.*, 2008, **92**, 063507.

17 R. Cohen, *Nature*, 1992, **358**, 136.

18 C. Duan, S. Jaswal and E. Tsymbal, *Phys. Rev. Lett.*, 2006, **97**, 047201.

19 M. Niranjan, J. Velev, C. Duan, S. Jaswal and E. Tsymbal, *Phys. Rev. B*, 2008, **78**, 104405.

20 K. Yamauchi, B. Sanyal and S. Picozzi, *Appl. Phys. Lett.*, 2007, **91**, 062506.

21 J. Dai, H. Zhang and Y. Song, *J. Magn. Magn. Mater*., 2012, **324**, 3937.

22 W. Choi, D. Jeong, S. Seo, Y. Lee, T. Kim, S. Jang, H. Lee and K. Myung-Whun, *Phys. Rev. B*, 2011, **83**, 195113.

23 J. Garcia-Barriocanal, J. Cezar, F. Bruno, P. Thakur, N. Brookes and C. Utfeld, *Nat. Commun.*, 2010, **1**, 82.

24 H. Béa, M. Bibes, S. Cherifi, F. Nolting and B. Warot-Fonrose, *Appl. Phys. Lett.*, 2006, **89**, 242114.

25 S. Ju, T. Cai, G. Guo and Z. Li, *J. Appl. Phys.*, 2008, **104**, 053904.

26 W. Kohn and L. Sham, *Phys. Rev.*, 1965, **140**, A1133.

27 P. Blöchl, *Phys. Rev. B*, 1994, **50**, 17953.

28 G. Kresse and J. Furthmüller, *Phys. Rev. B*, 1996, **54**, 11169.

29 J. Perdew, K. Burke and M. Ernzerhof, *Phys. Rev. Lett.*, 1996, **77**, 3865.

30 H. Yang, C. Jin, W..Mi, H. Bai and G. Chen, *J. Appl. Phys.*, 2012, **112**, 063925.

31 P. Mohn and S. Mater, *J. Magn. Magn. Mater.*, 1999, **191**, 234.

32 M. Nolan and G. Watson, *Surf. Sci*., 2005, **586**, 25.

33 J. Padilla and D. Vanderbilt, *Phys. Rev. B*, 1997, **56**, 1625.

34 W. Mi, Z. Guo, X. Feng and H.Bai, *Acta Mater.*, 2013, **61**, 6387.

35 J. Wang, J. Neaton, H. Zheng, V. Nagarajan, S. Ogale, B. Liu, D. Viehland, V. Vaithyanathan, D. Schlom, U. Waghmare, N. Spaldin, K. Rabe, M. Wutting and R. Ramesh, *Science*, 2003, **299**, 1719.

36 H. Tütüncü and G. Srivastava, *Phys. Rev. B*, 2008, **78**, 235209.

37 D. Wang, W. Goh, M. Ning and C. Ong, *Appl. Phys. Lett.*, 2006, **88**, 212907.

38 N. Pertsev, A. Zembilgotov and A. Tagantsev, *Phys. Rev. Lett.*, 1998, **80**, 1988.

39 O. Diéguez, K. Rabe and D. Vanderbilt, *Phys. Rev. B*, 2005, **72**, 144101.

40 J. Von Appen and R. Dronskowski, *Angew. Chem. Int. Ed.*, 2005, **44**, 1205.

41 R. Coehoorn, G. Daalderop and H. Jansen, *Phys. Rev. B*, 1993, **48**, 3830.

42 E. Zhao, H. Xiang, J. Meng and Z. Wu, *Chem. Phys. Lett.*, 2007, **449**, 96.

43 Z. Lv, Y. Gao, S. Sun, M. Qv, Z. Wang, Z. Shi and W. Fu, *J. Magn. Magn. Mater.*, 2013, **333**, 39.

44 B. Frazer, *Phys. Rev.*, 1958, **112**, 751.

45 A. Schleife, F. Fuchs, J. Furthmüller and F. Bechstedt, *Phys. Rev. B*, 2006, **73**, 245212.

46 J. Dresner, *J. Appl. Phys.*, 1977, **48**, 4760.

47 R. Palai, R. Katiyar, H. Schmid, P. Tissot, S. Clark, J. Robertson, S. Redfern, G.

Catalan and J. Scott, *Phys. Rev. B*, 2008, **77**, 014110.

48 Y. Shi, Y. Du and G. Chen, *Solid State Commun.*, 2012, **152**, 1581.

49 Y. Shen, *Annu. Rev. Phys. Chem.*, 1989, **40**, 327.

50 R. Tung, *Phys. Rev. B*, 2001, **64**, 205310.

51 J. Tersoff, *Phys. Rev. Lett.*, 1984, **52**, 465.

52 D. Geppert, A. Cowley and B. Dore, *J. Appl. Phys.*, 1966, **37**, 2458.

TABLE NOTES

TABLE I. The calculated magnetic moment $m(\mu_B)$ of per atom in the Fe_4N/MgO supercell for models a and b as compared to bulk.

Model \ Atom	Layer	Fe^I	Fe^{II}	N	Mg	O
a	Bulk	2.95	2.31	0.02	0	0
	I	2.98	-0.23	—	0	(2)0.03 (6)-0.01
	II	—	(3)2.27 (4)2.35	-0.02	0	0
	III	2.97	2.84	—	0	0
b	I	—	2.63	-0.03	0	0
	II	2.73	1.33	—	0	0
	III	—	2.65	-0.03	0	0

TABLE II. Cohesive energy E_{coh} (eV) and optimized bond lengths d (Å) for the $Fe_4N/BaTiO_3$ and $Fe_4N/BiFeO_3$ interfaces.

Interface	$Fe_4N/BaTiO_3$				$Fe_4N/BiFeO_3$			
	a	b	c	d	a	b	c	d
Ba(Bi)-Fe^{I}	2.90	—	—	—	2.51	—	—	—
O-Fe^{I}	3.75	2.87	—	—	3.70	3.79	—	—
Ti(Fe)-Fe^{I}	—	3.54	—	—	—	3.76	—	—
Ba(Bi)-Fe^{II}	3.58	—	4.49	—	3.33	—	2.96	—
O-Fe^{II}	1.89	3.13	4.55	2.13	1.95	3.67	3.59	3.03
Ti(Fe)-Fe^{II}	—	2.61	—	2.91	—	2.60	—	—
Ba(Bi)-N	—	—	4.62	—	—	—	3.41	2.70
O-N	—	—	3.80	2.79	—	—	2.96	2.38
Ti(Fe)-N	—	—	—	2.03	—	—	—	
E_{coh}	-1.52	-0.73	-0.92	-2.31	-1.07	8.33	1.67	3.31

TABLE III. The calculated magnetic moment $m(\mu_B)$ of per atom in the $Fe_4N/BaTiO_3$ supercell for models a-d as compared to bulk.

Model \ Atom	Layer	Fe^I	Fe^{II}	N	Ba	Ti	O
	Bulk	2.95	2.31	0.02	0	0	0
	I	2.72	2.64	—	0.02	—	0.11
a	II	—	2.14	0.01	—	-0.05	0.01
	III	2.95	2.84	—	0	—	0
	I	3.12	2.49	—	—	-0.25	0.05
b	II	—	2.09	-0.02	0	—	-0.01
	III	2.92	2.58	—	—	-0.02	0.01
	I	—	2.49	-0.03	0	—	0.01
c	II	2.76	1.34	—	—	0	0
	III	—	2.51	-0.03	0	—	0
	I	—	2.53	0	—	-0.03	0.04
d	II	2.81	1.08	—	0	—	0.01
	III	—	2.46	-0.06	—	0.01	0

TABLE IV. The calculated magnetic moment $m(\mu_B)$ of per atom in the $Fe_4N/BiFeO_3$ supercell for models a-d as compared to bulk.

	Layer	Fe^{I}	Fe^{II}	N	Bi	Fe	O1	O2
	Bulk	2.95	2.31	0.02	0	±4.18	-0.21	0
	I	2.39	2.63	—	-0.20	—	(3)0.03 (6)0.09	—
	II	—	2.11	0.01	—	(2)-4.15 (4)4.16	—	-0.01
a	III	2.96	2.88	—	(2)0 (5)-0.01	—	(2)-0.05 (5)0.05	—
	IV	—	—	—	—	(1)4.15 (3)-4.15	—	0
	V	—	—	—	(1)-0.01 (4)0.01	—	(1)0.10 (4)-0.10	—
	I	2.98	2.46	—	—	(3)3.86 (6)-3.82	—	0
	II	—	(5/6)1.61 (7/8)1.68	(1)-0.03 (2)0	(2)-0.01 (4)0.01	—	(2)-0.16 (4)0.16	—
b	III	2.92	(2)2.74 (4)2.84	—	—	(2)-4.16 (5)4.17	—	0.01
	IV	—	—	—	(1)0.01 (2)-0.01	—	(1)0.17 (3)-0.01	—
	V	—	—	—	—	(1)4.12 (4)-3.11	—	-0.32
	I	—	0.95	-0.06	-0.02	—	(3)-0.17 (6)0.01	—
	II	2.88	1.55	—	—	(2)-4.20 (4)3.37	—	-0.10
c	III	—	1.91	-0.07	-0.01	—	(2)0.11 (5)0.04	—
	IV	—	—	—	—	(1)4.14 (3)-3.54	—	0.03
	V	—	—	—	-0.01	—	(1)0.20 (4)0.12	—
	I	—	2.35	-0.04	—	(3)4.19 (6)-4.13	—	0.13
	II	2.79	0.91	—	(2)0.01 (4)-0.01	—	(2)0.13 (4)-0.13	—
d	III	—	2.35	-0.03	—	(2)-4.16 (5)4.18	—	-0.01
	IV	—	—	—	(1)-0.01 (3)0.01	—	(1)0.02 (3)0.19	—
	V	—	—	—	—	(1)4.16 (4)-3.65	—	0.07

FIGURE CAPTIONS

Fig. 1 The top, middle, and bottom planes are the supercell structures of Fe_4N/MgO, $Fe_4N/BaTiO_3$ and $Fe_4N/BiFeO_3$, respectively. The right side is corresponding side view of the three dimensional charge density difference plots and plane-averaged charge density difference along the vertical *z*-direction normal to the interface. Blue and yellow isosurfaces represent charge depletion and accumulation in the space with respect to isolated Fe_4N and oxides surface, respectively. Corresponding, blue color filled areas represent a charge depletion region and yellow color filled areas represent a charge accumulation region. The areas between the green dashed lines are the interfacial regions.

Fig. 2 PDOS obtained from fully relaxed models a and b in the Fe_4N/MgO interfaces, projected on different layers. (a) and (b) the PDOS of Fe_4N and MgO for model a, respectively; (c) and (d) the PDOS of Fe_4N and MgO for model b, respectively. The shaded plots are the DOS of atom in bulk crystal. Numbers in brackets denote the atoms at different site. E_F is indicated by the vertical line and E_F is set at 0 eV.

Fig. 3 (a) spin-unpolarized band structure of MgO; (b) and (c) the majority and minority spin band structure along high-symmetry direction in the two-dimensional Brillouin zone for model a in the Fe_4N/MgO interfaces,

respectively; (d) and (e) the majority and minority spin band structure along high-symmetry direction in the two-dimensional Brillouin zone for model b in the Fe_4N/MgO interfaces, respectively. The red color indicates the MgO contribution and gray denotes the Fe_4N contribution. E_F is set to zero.

Fig. 4 PDOS obtained from fully relaxed models a and b in the $Fe_4N/BaTiO_3$ interfaces, projected on different layers. (a) and (b) the PDOS of Fe_4N and $BaTiO_3$ for model a, respectively; (c) and (d) the PDOS of Fe_4N and $BaTiO_3$ for model b, respectively. The shaded plots are the DOS of atom in bulk crystal. E_F is indicated by the vertical line and E_F is set at 0 eV.

Fig. 5 PDOS obtained from fully relaxed models c and d in the $Fe_4N/BaTiO_3$ interfaces, projected on different layers. (a) and (b) the PDOS of Fe_4N and $BaTiO_3$ for model c, respectively; (c) and (d) the PDOS of Fe_4N and $BaTiO_3$ for model d, respectively. E_F is indicated by the vertical line and E_F is set at 0 eV.

Fig. 6 (a) spin-unpolarized band structure of $BaTiO_3$; (b)-(e) the band structure along high-symmetry direction in the two-dimensional Brillouin zone for models a-d in the Fe_4N/ $BaTiO_3$ interfaces, respectively; The top and bottom rows in (b)-(e) planes represent the majority and minority spin band structure, respectively. The red color indicates the $BaTiO_3$ contribution and gray denotes

the Fe_4N contribution. E_F is set to zero.

Fig. 7 PDOS obtained from fully relaxed models a and b in the $Fe_4N/BiFeO_3$ interfaces, projected on different layers. (a) and (b) the PDOS of Fe_4N and $BiFeO_3$ for model a, respectively; (c) and (d) the PDOS of Fe_4N and $BiFeO_3$ for model b, respectively. The shaded plots are the DOS of atom in bulk crystal. Numbers in brackets denote the atoms at different site. E_F is indicated by the vertical line and E_F is set at 0 eV.

Fig. 8 PDOS obtained from fully relaxed models c and d in the $Fe_4N/BiFeO_3$ interfaces, projected on different layers. (a) and (b) the PDOS of Fe_4N and $BiFeO_3$ for model c, respectively; (c) and (d) the PDOS of Fe_4N and $BiFeO_3$ for model d, respectively. Numbers in brackets denote the atoms at different site. E_F is indicated by the vertical line and E_F is set at 0 eV.

Fig. 9 (a) spin-unpolarized band structure of $BiFeO_3$; (b)-(e) the band structure along high-symmetry direction in the two-dimensional Brillouin zone for models a-d in the $Fe_4N/BiFeO_3$ interfaces, respectively; The top and bottom rows in (b)-(e) planes represent the majority and minority spin band structure, respectively. The red color indicates the $BiFeO_3$ contribution and gray denotes the Fe_4N contribution. E_F is set to zero.

Figure 1, Nan Feng *et al.*

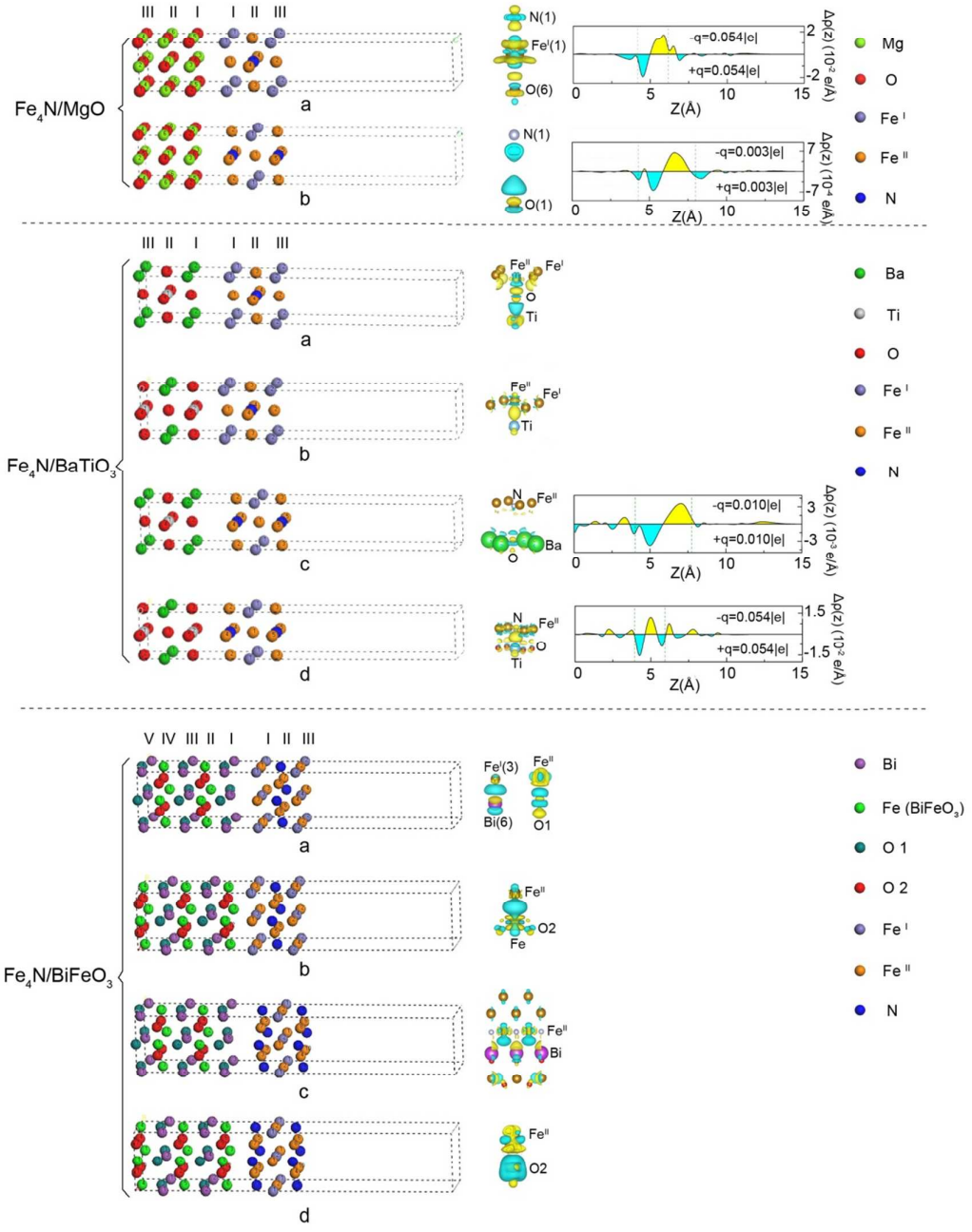

Figure 2, Nan Feng *et al.*

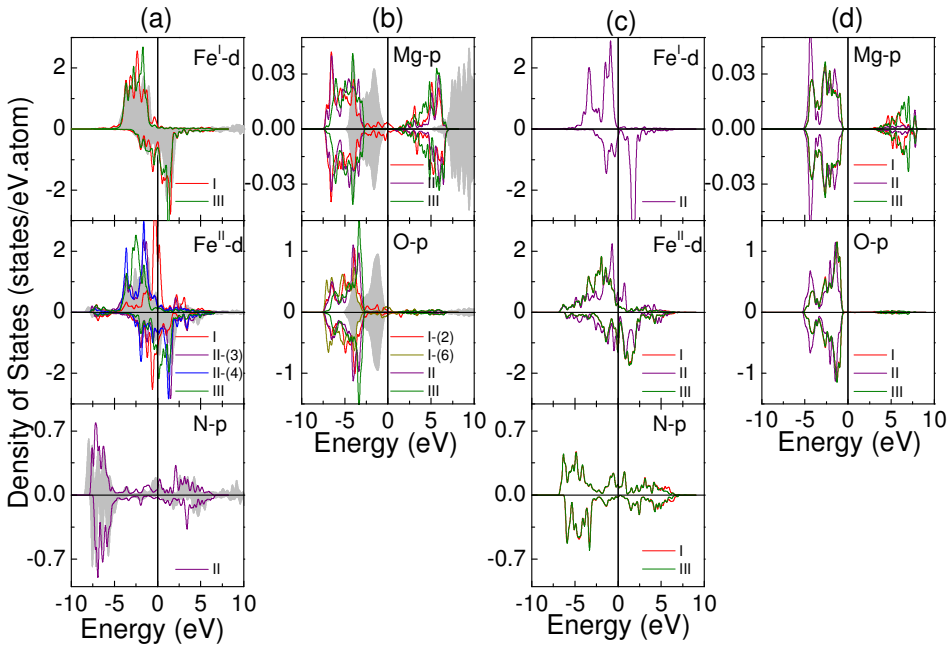

Figure 3, Nan Feng *et al.*

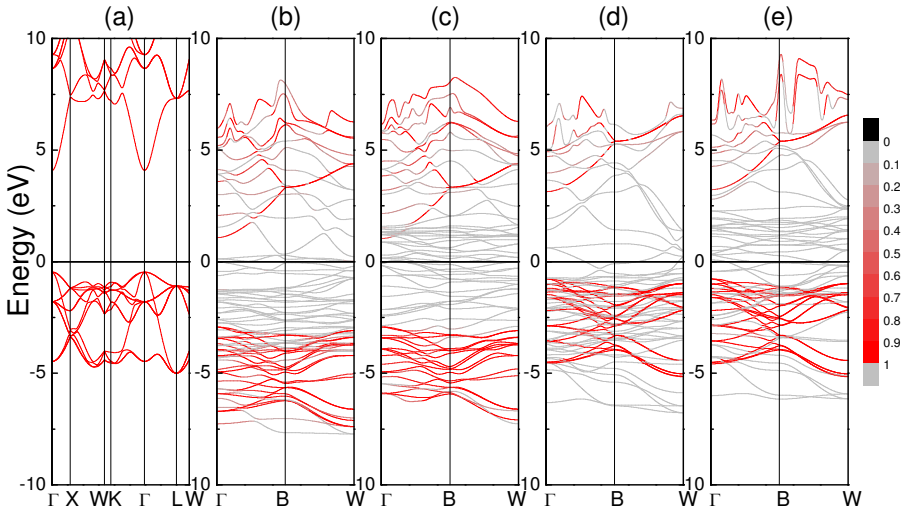

Figure 4, Nan Feng *et al.*

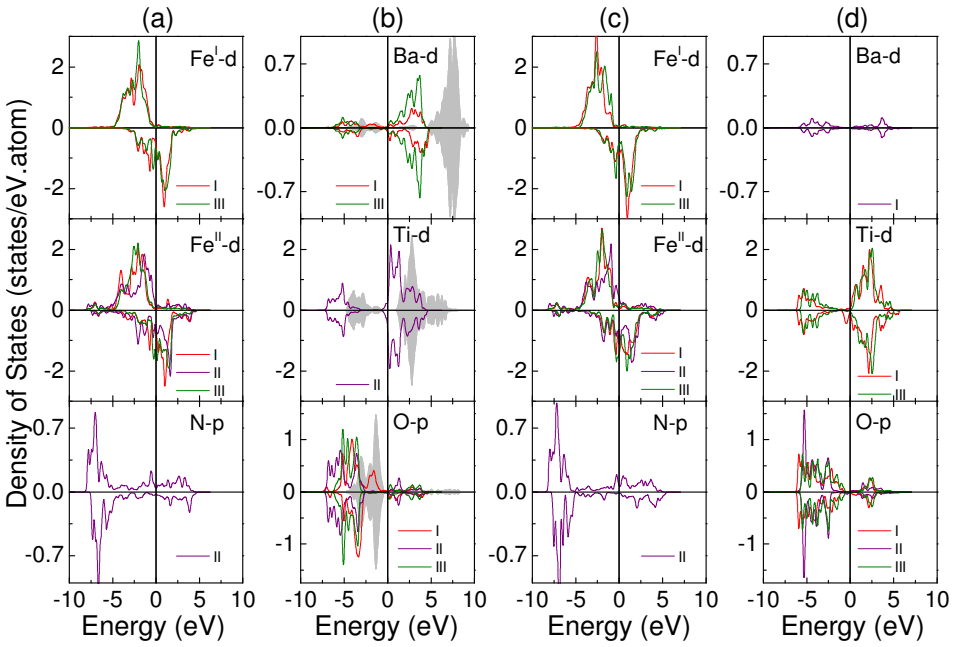

Figure 5, Nan Feng *et al.*

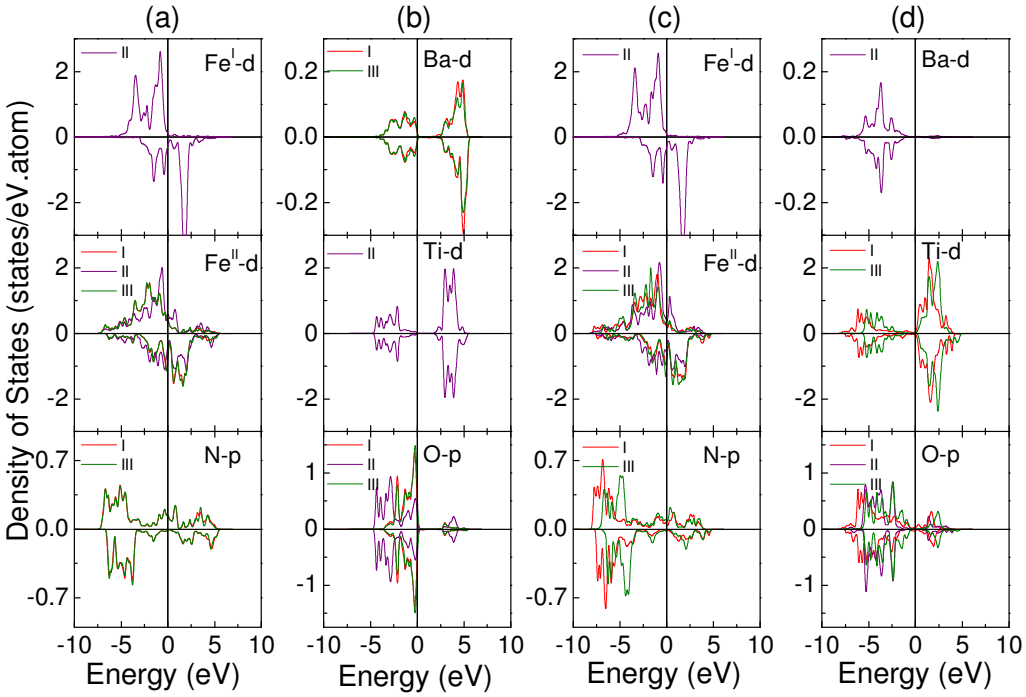

Figure 6, Nan Feng *et al.*

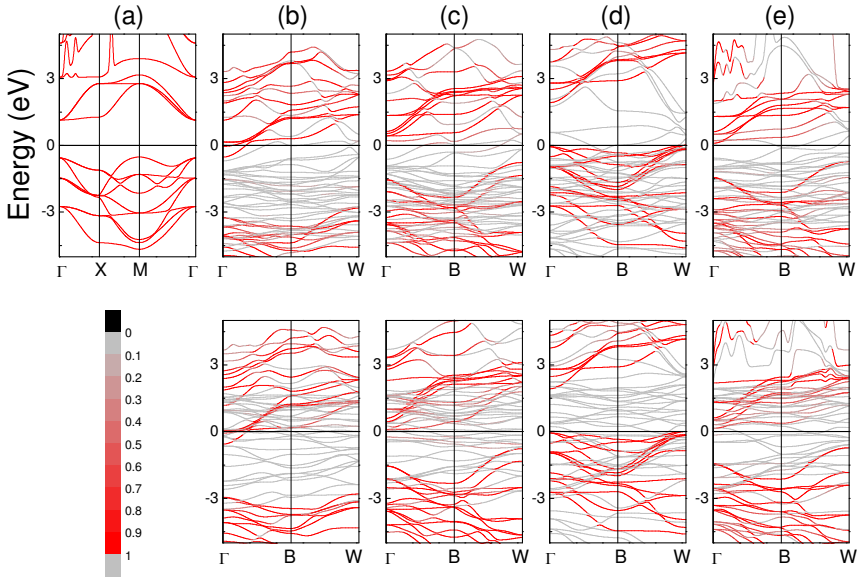

Figure 7, Nan Feng *et al.*

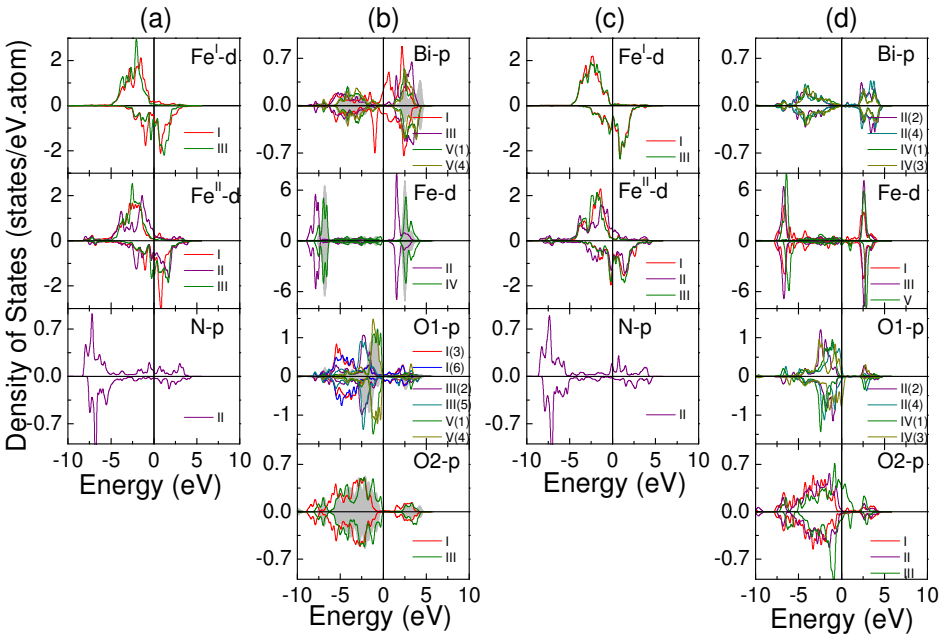

Figure 8, Nan Feng *et al.*

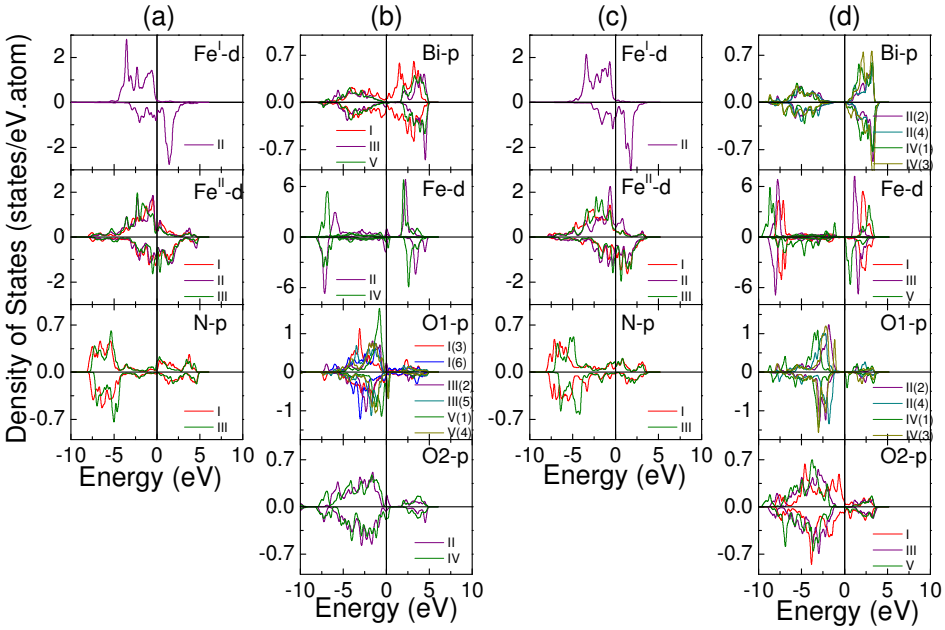

Figure 9, Nan Feng *et al.*

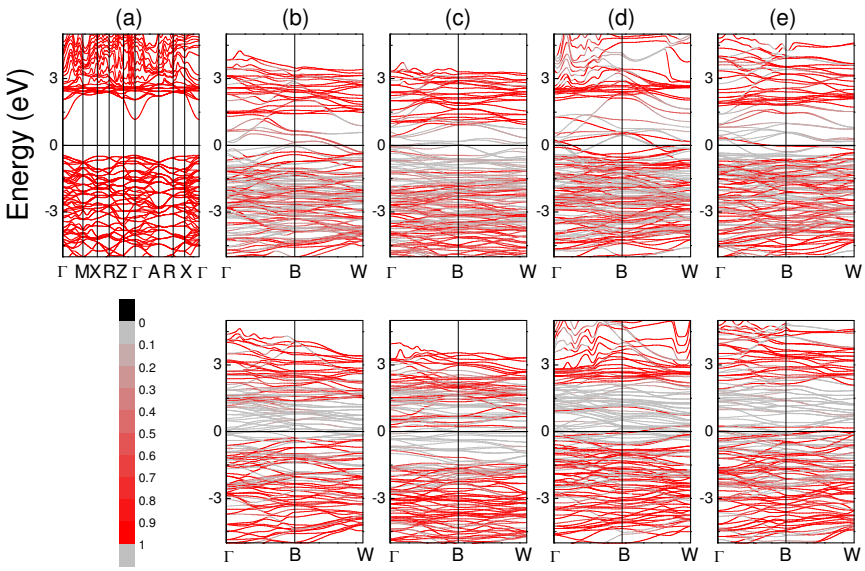

Graphical Abstract and Research Highlights

Graphical Abstract

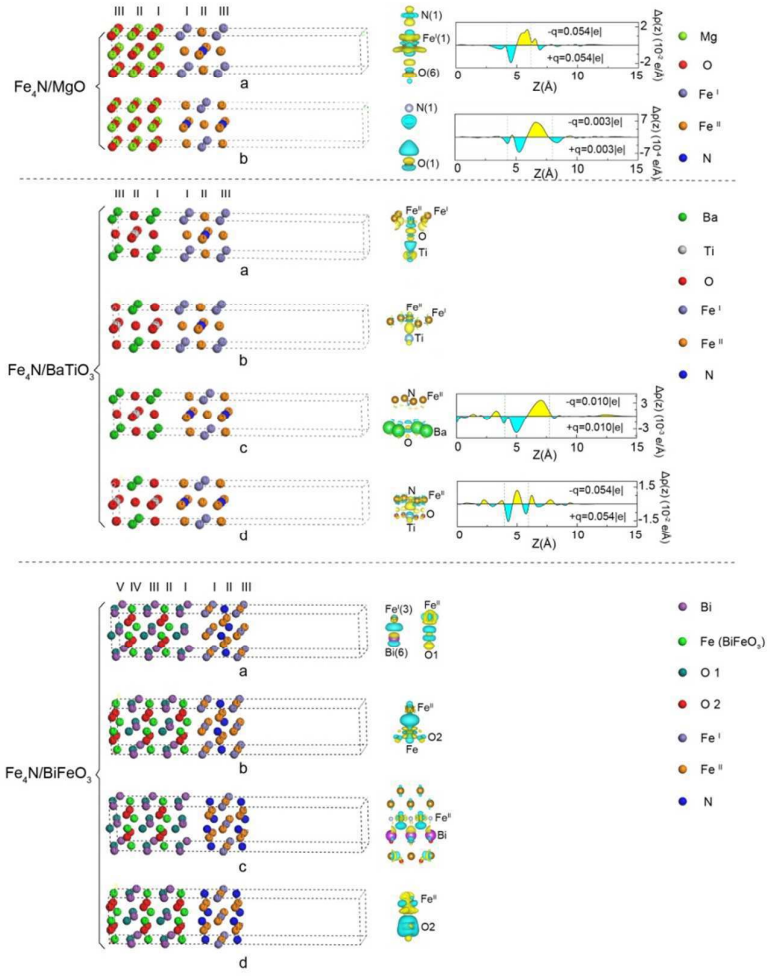

Highlights

(1) *n*- and *p*-type doping of MgO are induced in contact with $Fe^{I}Fe^{II}$ and $(Fe^{II})_2N$

terminations of Fe_4N, respectively.

(2) The metallic characters are induced in $BaTiO_3$ by contact with $Fe^{I}Fe^{II}$ termination, whereas *p*-type doping in $(Fe^{II})_2N/BaO$ interface and *n*-type doping in $(Fe^{II})_2N/TiO_2$ interface.

(3) The interfacial dipole due to charge rearrangement may induce the Fermi level pinning in Fe_4N/MgO and $(Fe^{II})_2N/BaTiO_3$ interfaces.

(4) The deposition of Fe_4N on $BiFeO_3$ can result in a metallic $BiFeO_3$.